Pure Appl. Geophys.

DOI 10.1007/s00024-017-1609-8

Pure and Applied Geophysics

Earthquake Triggering Inferred from Rupture Histories, DInSAR Ground Deformation and Stress-Transfer Modelling: The Case of Central Italy During August 2016–January 2017

G. A. Papadopoulos,[1] A. Ganas,[1] A. Agalos,[1] A. Papageorgiou,[1] I. Triantafyllou,[1] Ch. Kontoes,[2] I. Papoutsis,[2] and G. Diakogianni[2]

Abstract—On August 24, October 26 and 30, 2016, Central Apennines (Italy) were hit by three shallow, normal faulting very strong earthquakes rupturing in an NW–SE striking zone. Event 3 (Norcia) occurred between event 1 (Amatrice) at the SE and event 2 (Visso) at the NW of the entire rupture zone. The rupture histories of the three events, as revealed by teleseismic P-wave inversion, showed that all were characterized by bilateral rupture process with stronger rupture directivity towards NW for events 1 and 3 and towards SSE for event 2. Maximum seismic slip of 1.2, 0.8, and 1.4 m in the hypocenter and magnitude of M_w 6.2, 6.1, and 6.5 were calculated for the three events, respectively. DInSaR measurements based on Sentinel-1 and 2 satellite images showed ground deformation directivity from events 1 and 2 towards event 3, which is consistent with the rupture process directivity. For events 1, 2, and 3, the maximum ground subsidence was found equal to 0.2, 0.15, and 0.35 m. Based on rupture directivity and ground deformation pattern, we put forward the hypothesis that the area of the second event was stress loaded by the first one and that both the first and second earthquake events caused stress loading in the area, where the third event ruptured. Coulomb stress-transfer modelling yields strong evidence in favor of our hypothesis. The stress in the fault plane of event 2 was increased by $\sim$0.19 bars due to loading from event 1. Event 3 fault plane was loaded by an amount of $\sim$2 bars, due to the combined stress transfer from the two previous events, despite its proximity to the negative/positive lobe boundary. The three events produced combined stress loading of more than +0.5 bar along the Apennines to the NW and SE of the entire rupture zone. In the SE stress lobe, a series of strong earthquakes of M_w 5.3, 5.6, and 5.7 occurred on January 18, 2017, but likely, seismic potential remains in the area. We consider that in the NW and more extensive stress lobe, the seismic potential has also elevated due to stress loading.

Key words: Rupture histories, teleseismic P-wave inversion, stress transfer, DInSAR, central Italy, 2016–2017 earthquakes, earthquake triggering.

[1] Institute of Geodynamics, National Observatory of Athens, Athens, Greece. E-mail: papadop@noa.gr

[2] Institute for Astronomy, Astrophysics, Space Applications and Remote Sensing, National Observatory of Athens, Athens, Greece.

1. Introduction

The area of Central Apennines, Italy, is of high seismicity with long historical record of strong earthquakes. Before 2016, at least 16 earthquakes with magnitude exceeding 6.0 ruptured the area since the 13th century AD (Rovida et al. 2016) (Fig. 1). The last event was the lethal L'Aquila shock (M_w 6.3) of April 6, 2009. During the period August–October 2016, Central Apennines was hit by a series of strong earthquakes, three of them of magnitude >6. On August 24, 2016, the first strong earthquake of moment magnitude M_w 6.2 (Table 1) struck the area causing extensive destruction and a death toll of about 300 in the area defined by the towns of Norcia to the north and Amatrice to the south (Fig. 1). The seismicity rate remained at high level until another two strong shocks ruptured to the north on the October 26th, 2016 with M_w 6.1 the first and on the October 30th, 2016 with M_w 6.5 the second (Table 1). All the events were associated with normal faulting striking NNW–SSE with dip to SW (Table 2). On January 18, 2017, the strong earthquake activity repeated with a series of shocks, the three largest measuring magnitudes M_w 5.3, 5.7, and 5.6, all occurring at the SE prolongation of the zone activated with the earthquake of August 24, 2016.

As regard the first strong earthquake of August 24, some first results already appeared. Investigations included the co-seismic geological effects (Pucci et al. 2016) and surface ruptures (Albano et al. 2016) as well as the faults activated (Falcucci et al. 2016). In addition, the possible impact of the August 24, 2016 Amatrice earthquake on the seismic hazard assessment in central Italy was statistically examined

Published online: 05 July 2017

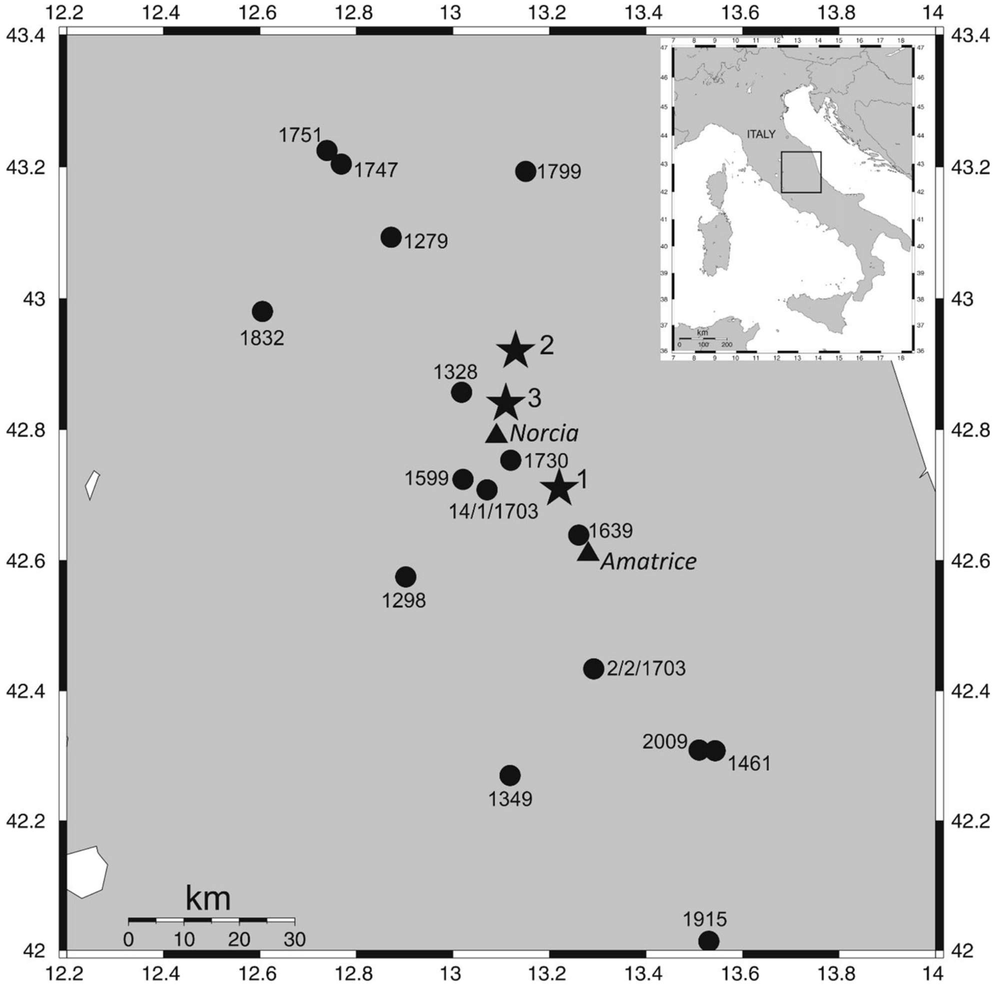

Figure 1

Earthquakes of magnitude exceeding 6.0 that occurred in the area of Central Apennines (Italy) from the 13th century up to the present (data taken from the CPTI15 historical earthquake data base of INGV by Rovida et al. 2016). Key: *solid circles* historical earthquake epicentres, figure near *solid circle* year of earthquake occurrence, *stars* epicentres of the three largest earthquakes occurring in 2016 (1 for August 24, 2 for October 26, and 3 for October 30), *solid triangle* town

Table 1

Focal parameters of the three largest earthquakes in Central Apennines (Italy) during August–October 2016 as determined by INGV (http://cnt.rm.ingv.it) except magnitudes which are explained below

No.	Date	Time	LAT	LONG	h (km)	M_w (1)	M_w (2)	M_w (3)
1	August 24, 2016	01:36:32	13.2335	42.6983	8.10	6.00	6.20	6.20
2	October 26, 2016	19:18:05	13.1288	42.9087	7.50	5.90	6.10	6.10
3	October 30, 2016	06:40:17	13.1100	42.8400	9.40	6.50	6.60	6.50

LAT, LON, and h are geographical latitude and longitude of the epicentre and focal depth, respectively. Moment magnitude M_w (1), M_w (2), and M_w (3) are taken from INGV, Harvard CMT solutions (http://www.globalcmt.org/CMTsearch.html) and GFZ (http://geofon.gfz-potsdam.de/eqinfo/list), respectively

Table 2

Parameters regarding the P-wave teleseismic inversion of the three strong earthquakes

Date	L (km)	d (km)	v (km/s)	t (s)	h (km)	Rake	Rake range	Strike/dip	M_o (Nm)	M_w
August 24	27	12	2.8	0.9	7	−76	−46 to −106	157/43	2.2×10^{18}	6.2
October 26	27	12	2.7	0.8	7	−66	−36 to −96	169/46	1.8×10^{18}	6.1
October 30	40	12	2.9	1.1	7	−88	−58 to −118	158/44	6.6×10^{18}	6.5

Parameters inserted: L and d = fault length and width of the rectangular fault plane used for discretization of the sub-faults; strike, dip, and rake of the seismic fault are based on the GFZ solutions (http://geofon.gfz-potsdam.de/eqinfo/list); v and t are optimum rupture velocity and rise time, respectively. Key for parameters received: M_o seismic moment, M_w moment magnitude

by Murru et al. (2016). On the other hand, the slip heterogeneity and directivity of the Amatrice earthquake was approached by rapid finite-fault inversion and found that the first shock ruptured an NNW–SSE striking and WSW dipping normal fault (Tinti et al. 2016). This was also the case of the other two strong earthquakes as it results from moment tensor inversions (e.g., Pondrelli et al. 2016). Tinti et al. (2016) inverted waveforms from 26 three-component strong motion accelerometers, filtered between 0.02 and 0.5 Hz, within 45 km from the fault. The inferred slip distribution was found heterogeneous being characterized by two slip patches up–dip and NW from the hypocenter, respectively. A bilateral rupture propagation pattern with relatively high rupture velocity of 3.1 km/s was suggested by Tinti et al. (2016). They also supported that the imaged rupture history produced evident directivity effects both NNW and SE of the hypocenter, which is consistent with the analysis of accelerometric data by Saccorotti et al. (2016). On the other hand, Lavecchia et al. (2016) investigated the ground deformation and source geometry of the August 24, 2016 Amatrice earthquake by exploiting ALOS2 and Sentinel-1 co-seismic DInSAR measurements. They extended their analysis by applying a 3D finite-element approach jointly exploiting DInSAR measurements and an independent, structurally constrained, 3D fault model. They concluded that their hypothesis of a bilateral rupture propagating along two en echelon faults connected at the hypocenter and striking NNW–SSE is well supported (see also Bignami et al. 2016).

The impressive sequential rupture in Central Apennines with a series of strong earthquakes occurring in a time interval of only a few months raises some important issues. Do they share similar rupture processes? What has been the role of possible triggering effects? How the level of seismic potential has been affected by changes in the stress field of the area? This paper aims to approach such issues which are of crucial importance for the seismic hazard assessment in the area. We approached these issues by analyzing the rupture histories of the three strongest earthquake events with the inversion of teleseismic P-wave records along with differential interferometric synthetic aperture radar (DInSAR) measurements and results obtained from modelling of Coulomb stress transfer.

2. Rupture Histories

2.1. Data Used and Methodology for Slip Inversion

All three strong earthquake events, which occurred in Central Apennines on August 24, 2016 as well as on October 26 and October 30, 2016, were associated with normal faulting striking NNW–SSE and dipping towards WSW (Table 2). This is consistent with the regional tectonics of the area and surface ruptures (e.g., Albano et al. 2016; Falcucci et al. 2016). Alternative hypotheses on the surface ruptures and the tectonic framework can be found in Bonini et al. (2016) and Huang et al. (2017). The co-seismic slip models for the three events were retrieved from inversion of P waves recorded at teleseismic distances ranging from 30° to 90°. Waveforms from 30 stations with good azimuthal coverage (Fig. 2) were used in each case. However, records with no clear signal (signal-to-noise ratio < 2) were not utilized.

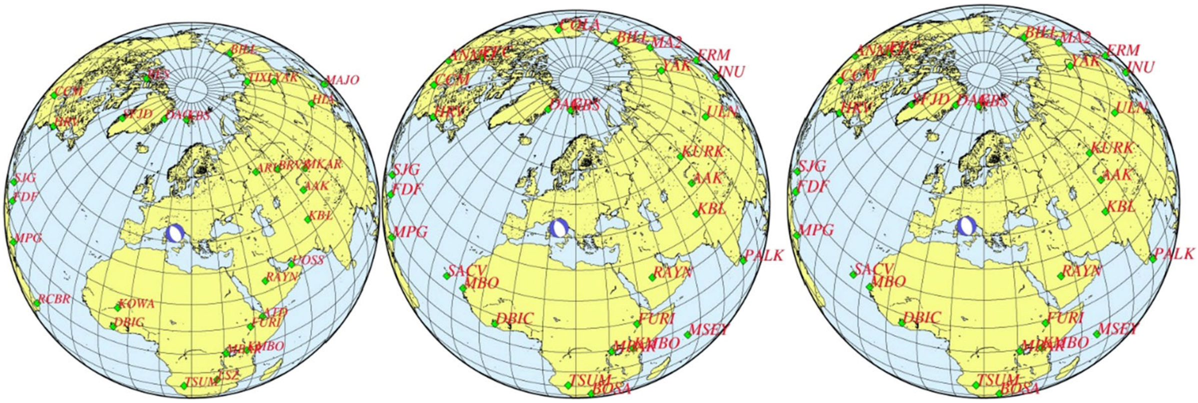

Figure 2

Geographical distribution of the stations used for the teleseismic P-wave inversion for the strong earthquakes of August 24 (*left*), October 26 (*center*), and October 30 (*right*), 2016

The waveforms were downloaded from the Iris Data Management Center (i.e., data from GSN, II, IU, and GE digital networks were used) using the Wilber 3 application. All waveforms were processed to remove the mean offset and instrument response, band-pass filtered between 0.02 and 1 Hz using a Butterworth filter, re-sampled to 0.2 samples/s, and finally integrated in time to obtain displacements.

The kinematic finite-fault inversion scheme of Hartzell and Heaton (1983) and Mendoza and Hartzell (2013), which is a non-negative, least squares inversion method, has been applied to produce the spatial and temporal evolutions of the slip on the ruptured fault. The application of the inversion method starts by constructing a rectangular fault plane which is discretized to a number of uniform cells which are called sub-faults. The point source responses were computed with a code based on the generalized ray theory (Langston and Helmberger 1975). The exact way these synthetics were constructed followed the discussion in the study of Heaton (1982). The calculated elementary synthetics were convolved with an attenuation operation under the assumption that $t^* = 1$ s for P waves, where t^* is the attenuation parameter of teleseismic body waves that represents the total body wave travel time divided by Q along the ray path (Stein and Wysession 2003).

The strike, dip, and rake of the seismic fault as well as the depth at the hypocenter are the source parameters needed as input to produce the elementary synthetics taking into account the time delays for a rupture front propagating with a prescribed rupture speed. The amount of slip in successive time intervals for each sub-fault is lagged in time by the width of the source. As described by Hartzell and Langer (1993), the constructed rise time functions are free to vary as a function of position on the fault plane. The followed finite-fault inversion approach, with the use of the multiple time windows, permits the same sub-fault to rupture multiple times. The final rise time is obtained by the summation of the individual rise time functions for each time window. The fit between data and synthetics is shown in the Appendix (Figs. 11, 12, 13).

2.2. Fault Parameterization

For the series of earthquakes examined several values of source velocity, varying from 2.6 to 3.3 km/s, rise time, fault dimensions and time lag were tested. For each earthquake event, the source of the elementary synthetics was taken as of trapezoidal shape and the width of the source was chosen to be short enough compared to the total rise time on the fault. The faults were discretized by 108 sub-faults, 18 of them along strike and 6 along dip. The sub-fault synthetics were computed using the velocity model of Herrmann et al. (2011) for Central Apennines. For the kinematic inversion of these three earthquakes, we

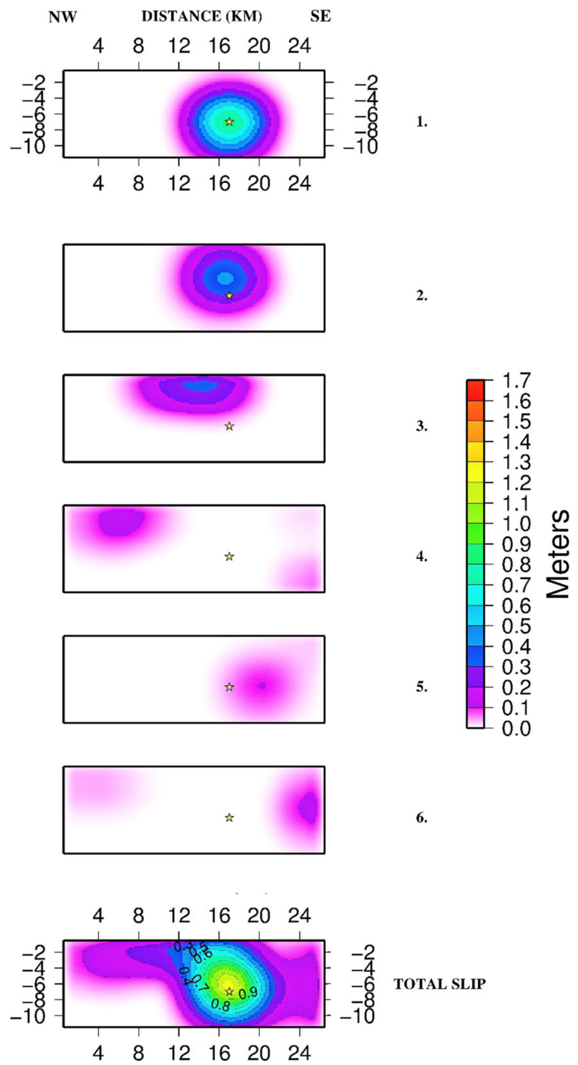

Figure 3
Seismic slip history for the strong earthquake of August 24, 2016 in six snaps using time intervals of 1.7 s. Results are explained in Sect. 2.3

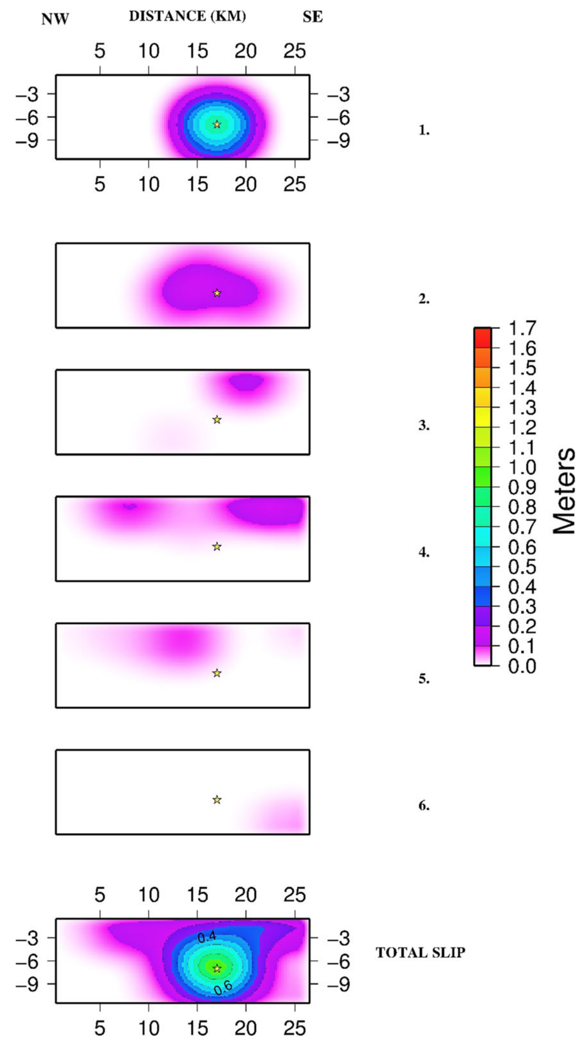

Figure 4
Seismic slip history for the strong earthquake of October 26, 2016 in six snaps using time intervals of 1.5 s. Results are explained in Sect. 2.3

used the strike, dip, and rake parameters from the GFZ focal mechanism solutions taking the nodal plane with NW–SE direction and dipping to SW as the fault plane ruptured. The parameters used for, and obtained by, the inversion procedure for each one of the three cases are listed in Table 2. We fixed the fault geometry based on the GFZ parameters and we did not have to compare the misfit of fault parameters with all other solutions available (e.g., GCMT, USGS, and INGV) as the differences between them were very small (Pondrelli et al. 2016; for fault-plane solutions comparison see also in EMSC, http://www.emsc-csem.org/#2). To make the rake vary upon the fault, we followed the suggestion by Hartzell et al. (1996) and calculated the synthetics twice with ±30° from the initial rake (Table 2) using six time windows for the inversion process, each one of them having a duration equal to the rise time. We considered the rise time to lightly change with the magnitude of the events allowing for all cases the dislocation duration to be long enough to span the range of expected rise times for earthquakes of this size (Somerville et al. 1999).

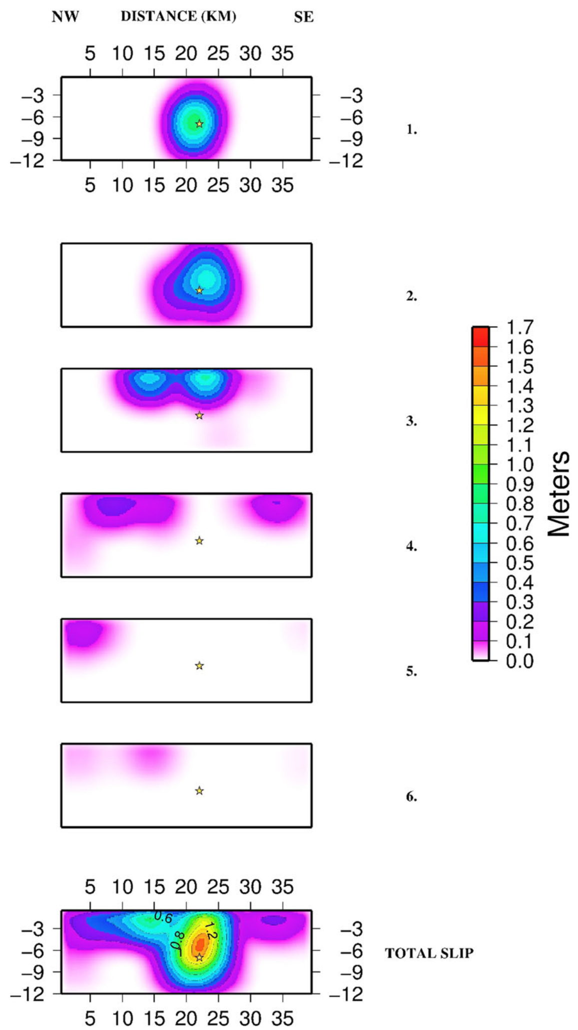

Figure 5
Seismic slip history for the strong earthquake of October 30, 2016 in six snaps using time intervals of 2.0 s. Results are explained in Sect. 2.3

2.3. Slip Distribution

The co-seismic slip distribution of the three earthquakes, representing the movement of the hanging wall in respect to the foot wall, is illustrated in Figs. 3, 4, and 5. The time evolution of slip is presented in each case by six snaps using nearly 1.7-, 1.5-, and 2.0-s intervals for the events of August 24, October 26, and October 30, 2016, respectively. The slip distributions are smooth as a 2D cone shaped filter was applied. The simplest solution plotted is the one succeeded using a trial-and-error process that balances fitting the data by the Residual Norm $\|Ax - b\|$, with smoothing and minimizing the slip (Mendoza and Hartzell 2013), where A is the sub-fault synthetics matrix, b is the matrix of observations, and x is the solution vector containing the slip required to reproduce the observations.

The rupture history of the August 24 earthquake (Fig. 3) shows bilateral propagation mode with strong rupture directivity, which is consistent with the results of Lavecchia et al. (2016), Lanzano et al. (2016) and Tinti et al. (2016). The rupture started at the hypocenter's depth and evolved up–dip. The co-seismic slip took its maximum value of about 1.2 m close to the hypocenter at a depth of 7 km. The rupture moved mainly towards NW being concentrated in a very shallow layer at depths between 2 and 5 km with seismic slip of about 0.3 m near the surface. This is consistent with the co-seismic ruptures observed by the EMERGEO Working Group (Pucci et al. 2016) down-throw the SW side of bedrock in the Mt. Vettore Fault System at the north of the earthquake rupture zone with vertical displacement being mostly below 16 cm and exceeding 35 cm in few locations of its northern portion. High-rate GPS records at epicentral distances of $\sim$9 km to the SE and $\sim$14 km to the NW showed larger values of peak-to-peak displacements on the radial component ($\sim$16.6 cm) and on the transverse component ($\sim$15.0 cm), respectively (Avallone et al. 2016). According to our inversion, the rupture directed also towards SE covering smaller area and shorter distance relative to the NW side, which is consistent with the analysis of accelerometric data by Saccorotti et al. (2016). This indicates that the rupture directivity was much stronger towards NW, where possibly was associated with a second patch in the imaged ground velocity inversion shown by Tinti et al. (2016). Main directivity effect towards NW was also revealed by the accelerometric data of Lanzano et al. (2016) and Pischiutta et al. (2016). The rupture had a length of nearly 13 km. The seismic moment calculated was found 2.2×10^{18} Nm which corresponds to magnitude M_w 6.2. This is consistent with M_w calculations by others (Table 1).

The rupture history of the October 26, 2016 earthquake (Fig. 4) revealed that this earthquake had also bilateral propagation but smaller seismic slip and rupture length relative to the strong earthquake of

August 24. The rupture started with maximum slip values of about 0.8 m at the hypocenter's depth and continued upwards. The slip likely reached close to the Earth's surface with small slip values of no more than 0.1 m. The rupture length was of ~ 12 km. The rupture of this earthquake, in contrast to that of August 24, had stronger directivity towards SSE. The seismic moment was found 1.8×10^{18} Nm which corresponds to M_w 6.1.

Strong complexity and again a bilateral rupture propagation was revealed by the rupture history of the October 30 earthquake (Fig. 5). The main rupture, having maximum seismic slip of nearly 1.4 m, started at depth of ca. 5.5 km and propagated upwards close to the Earth's surface, where the slip ranged from 0.1 to 0.7 m. The rupture directivity was much stronger towards NW, where a secondary slip patch became evident with seismic slip of about 0.7 m at depth of ca. 3 km and at distance of about 8 km to the north of the main rupture. A small slip patch possibly ruptured about 10 km to the SE of the main rupture. The total rupture had a length of nearly 17 km. Seismic moment of 6.6×10^{18} Nm was found which corresponds to M_w 6.5. This is consistent with other M_w calculations (Table 2).

The three rupture histories examined had some common features such as rupture velocities which ranged from 2.7 to 2.9 km/s and bilateral rupture propagation with stronger directivity to a specific direction which is the same for the August 24 and October 30 earthquakes, that is from SE to NW, while for the October 26 event, the directivity was stronger towards SE. The rupture rise time was 0.9, 0.8, and 1.1 s for the August 24, October 26, and October 30, 2016 earthquakes, respectively. Rise time is the time needed for a single particle on the fault to achieve its final displacements. Since displacement is a function of magnitude and the rupture velocity increased with magnitude, it is reasonable to expect rise time to increase also with magnitude (Somerville et al. 1999).

3. Ground Deformation from DInSAR Based on Sentinel Imageries

3.1. Measurements and Methodology

Shortly after all the three earthquake occurrences, BEYOND Center of Excellence (http://

Table 3

Characteristics of the interferometric pairs processed and for which the corresponding displacement maps are presented in Fig. 6

Figure 6 map	Master date	Master satellite	Slave date	Slave satellite	Heading	Incidence angle at centre swath	Temporal baseline (days)	Perpendicular baseline (m)	Height of ambiguity h_a (m)	Doppler shift (Hz)
A	August 22, 2016	S1A	August 28, 2016	S1B	Ascending	39.5°	6	29	536	−120
B	October 21, 2016	S1A	October 27, 2016	S1B	Ascending	39.5°	6	67	230	−54
C	October 27, 2016	S1B	November 02, 2016	S1A	Ascending	39.3°	6	20	769	33
D	October 20, 2016	S1A	November 01, 2016	S1A	Descending	39.4°	12	119	130	−12

Height of ambiguity corresponds to the elevation change (in meter) to produce one fringe in the interferogram. In the case of DInSAR, this value corresponds to the DEM error that will erroneously produce one deformation fringe. Unfortunately, no descending pass combination was possible that would include and isolate only the October 30, 2016 earthquake. Therefore, pair D will contain phase contribution from both the October 26 and October 30, 2016 earthquakes beyond-eocenter.eu/), established at the National Observatory of Athens (NOA), acquired and processed Sentinel-1A and Sentinel-1B Single Look Complex (SLC) imagery, acquired in TOPS Interferometric Wide Swath mode. The SAR data were retrieved from the Hellenic National Sentinel Data Mirror Site (https://sentinels.space.noa.gr/), an ESA Collaborative Ground Segment operated by NOA and powered by a dedicated high bandwidth GEANT communication link operated by GRNET (the Greek partner of GEANT). Table 3 provides detailed information on the Sentinel data processed. The 6-day short revisit time and the short orbital tube of the mission, secure suppression of the temporal and geometric decorrelation. In addition, the high height of ambiguity (h_a) of the interferometric pairs corresponds to reduced sensitivity to digital elevation model (DEM) errors. For the subtraction of the DEM contribution in the interferometric phase, we used an SRTM V4 digital elevation model (Farr and Kobrick 2000) with nominal accuracy of ± 20 m in steep slopes, well below h_a for all pairs.

The SLC SAR imagery was processed using the SARscape commercial software package from sarmap. Interferogram filtering was done using the approach developed by Goldstein and Werner (1998), while phase unwrapping was performed with the Minimum Cost Flow algorithm (Costantini 1998) with the aid of Ground Control Points, manually selected in non-deforming, flat slope regions. It is worth noting that the deformation is measured along the observation line-of-sight (LOS). In the ascending pass, the satellite moves almost perfectly from south to north (azimuth direction, approximately 85°) and is looking right to the east. In the descending pass, the satellite moves from north to south (approximately −83°) and is looking right, to the west. The off-nadir viewing angle is variable in Sentinel-1, ranging from 18.3° to 46.8°. In this context, the LOS deformation measurement contains two motion components, the movement in the vertical direction and the movement in the east–west direction. The sensitivity of the interferometer in the north–south direction is nearly negligible.

3.2. *Results and interpretation*

The displacement pattern derived for the three ascending interferometric pairs that independently contain the three strong earthquakes (Fig. 6a–c) is remarkably similar. As one moves from east to west, the deformation sign moves from negative to positive. This is a first indication that the earthquake mechanism and likely the fault geometry were the same for all three shocks, which is the case as indicated by the earthquake fault-plane solutions (Table 2). Analyzing the August 24th event, the maximum negative ascending LOS deformation (Fig. 6a) is approximately −20 cm, observed west of Arquata del Tronto. The maximum positive ascending LOS deformation is +10-cm SSW of Accumoli. These values are comparable with the ones found by Lavecchia et al. (2016) but also with the displacement amplitude of up to 0.3 m found in the very shallow layer of 2–5 km from teleseismic P-wave inversion. The corresponding values for the October 26th event are −15- and +11.5-cm NE and SW of Visso, respectively. For the October 30th earthquake, the values are −35-cm NNW of Casteluccio and +24 cm at Norcia, respectively. Considering the descending pass that covers both these earthquakes (Fig. 6d), descending LOS deformation is in the range of −67 cm in Casteluccio and +22.5-cm east from Casteluccio. The displacement pattern associated with the descending pass (Fig. 6d) is dominated by the October 30th earthquake, although the pattern caused from the October 26th event is also evident near Visso. These deformation values are again consistent with the ones found in very shallow layers by our teleseismic P-wave inversion, ranging up to 0.1 m for event 2 and from 0.1 to 0.7 m for event 3.

The shape of the spatial displacement distribution for the August 24 and October 26, 2016 earthquakes shows that deformation in both events had a directivity towards the location, where the large earthquake of October 30 occurred. In fact, the deformation magnitude increases from south to north in Fig. 6a, while it increases from north to south in Fig. 6b. This is further supported by the rupture directivity but also from the stress-transfer modelling analyzed in the next section.

Assuming that the fault network and earthquake mechanism responsible for all three events is similar, we analyzed the synthetic deformation for the October 30 earthquake considering both ascending and descending passes. The conclusion will be applicable to the two prior events as well. In our case, normal faulting is common to the three cases.

Interpreting the complex motion of a deformed area as observed from two view angles, i.e., the ascending and descending LOS directions, is not straightforward (e.g., Boncori et al. 2015). In general, in normal faulting conditions, subsidence is observed in the hanging wall of the fault, which implies that vertical motion component prevails. Then, the LOS change is in the direction away from the satellite, i.e., by convention negative deformation for both heading passes. On the other hand, when the motion is predominantly in the eastward direction, then the LOS change in the ascending track would occur away from the satellite (negative), while for the ascending track, it would change towards the satellite (positive). Thus, a general rule of thumb would be that when motion of the same sign is detected by both descending and ascending tracks, then displacement in the vertical direction is dominant, while when opposite signs are encountered, east–west movement is more likely to be occurring.

In Fig. 6c, d, Casteluccio exhibits negative LOS deformation in both descending and ascending passes, implying that it subsided during the earthquake. The region in the vicinity of Norcia, on the other hand, has positive LOS deformation in the ascending pass and negative in the descending, implying a westward motion. In fact, the descending product can be used to identify the hanging wall and the footwall. Both Casteluccio and Norcia lay in the hanging wall side of the normal fault that deeps west (BB′ in Fig. 6 is the approximate surface fault trace). Starting a few kilometers east from Casteluccio (along BB′) and moving to the west, the descending pass shows the entire area with a negative LOS. This is in line with the fact that the area subsided but also moved to the west, i.e., both motion directions were away from the descending satellite.

In the ascending pass, however, there are two LOS zones, first negative (between BB′ and AA′) and then transitioning to positive (east of AA′). The transition boundary (AA′) lays in the middle between Casteluccio and Norcia. This gives us a better understanding of the actual (not LOS) deformation pattern. Again, starting a few kilometers east from Casteluccio (along BB′) and moving to the west up until the transition boundary (AA′), the area moves in two directions that are mapped with opposite signs in the ascending pass: subsidence (negative contribution to the observed LOS deformation in the ascending pass) and westward motion (positive contribution to the observed LOS deformation in the ascending pass). However, the amplitude of the subsidence contribution is much larger than that of the westward motion, and as a result, the zone exhibits negative LOS. As the subsidence amplitude decays moving from east to west (east of AA′), the westward contribution becomes equal and then greater than the subsidence contribution. Hence, the observed ascending LOS for this second zone is positive.

In the eastern area, where the footwall is situated west from BB′, the motion is more straightforward to derive; the uniformly opposite LOS signs for the descending and ascending passes suggest that the entire region moved to the east, which is consistent with the extensional regime of the area.

4. Coulomb Stress Transfer and Earthquake Triggering

Strong earthquakes can trigger subsequent earthquakes at short distances from the hypocenter by transferring static or dynamic stresses due to slip (e.g., Harris et al. 1995; Stein et al. 1997; Gomberg et al. 2001; Freed 2005; Parsons et al. 2006; Ganas et al. 2010). This interaction has been widely recognized on crustal faults. Correlations between earthquake occurrences and stress-transfer processes in Central Apennines and elsewhere in the Italian territory have been investigated by several authors (Cocco et al. 2000; Riva et al. 2000; Basili and Meghraoui 2001; Jacques et al. 2001; Dalla Via et al. 2003; Perniola et al. 2003; Ganas et al. 2012; Pace and Calamita 2014; Rovelli and Calderoni 2014). We investigated possible triggering effects due to stress transfer from the first earthquake of August 24, 2016 to the second and third strong events of October 26

Table 4

Principal stress axes as calculated using the NODAL/RAKE software (Louvari and Kiratzi 1997)

Date	Depth (km)	Strike/dip/rake plane 1	Strike/dip/rake plane 2	P-axis azimuth	P-axis plunge	T-axis azimuth	T-axis plunge
August 24	8	157°/43°/−76°	318°/49°/−103°	164°	80°	57°	3°
October 26	8	169°/46°/−66°	316°/49°/−113°	157°	73°	62°	2°
October 30	9	158°/44°/−88°	335°/46°/−92°	193°	88°	67°	1°

Slip models are after GFZ (http://geofon.gfz-potsdam.de/eqinfo/list)

and October 30, 2016 as well as from the second event to the third one. In addition, the potential for the generation of strong earthquakes due to the combined stress loading produced by the three earthquakes was also examined.

4.1. Stress-Transfer Methodology

We computed the Coulomb stress change in an elastic half space (Okada 1992) by assuming a shear modulus of 3.0×10^{10} Pa, Poisson's ratio 0.25, and effective coefficient of friction $\mu' = 0.4$. Details of the methodology can be found in previous works such as Ganas et al. (2008, 2010). The value of $\mu' = 0.4$ is a good compromise as it has been shown that by increasing the effective coefficient of friction, ΔCFF also increases (Ganas et al. 2010). In this simple modeling, we ignored pore pressure effects.

The change in the Coulomb failure function (ΔCFF, or Coulomb stress change) on target failure planes was calculated from the formula (Reasenberg and Simpson 1992):

$$\Delta \mathrm{CFF} = \Delta\tau + \mu' \Delta\sigma n, \tag{1}$$

where $\Delta\tau$ is the co-seismic change in shear stress on the receiver fault and in the direction of fault slip, $\Delta\sigma n$ is the change in the normal stress (with tension positive), and μ' is the effective coefficient of friction:

$$\mu' = \mu(1 - \Delta P/\Delta\sigma n), \tag{2}$$

where μ is the coefficient of static friction and ΔP is the pore pressure change within the fault. From (2), it follows that if $\Delta P = 0$, then $\mu' = \mu$. ΔCFF is the Coulomb stress change between the initial (ambient) stress and the final stress. If the dislocation model is thought of as an earthquake rupture, the ambient field is the field existing before the earthquake and the total field is the sum of the ambient field plus the earthquake-induced stresses. Failure on the target plane is enhanced if ΔCFF is positive, and is delayed if it is negative.

Figure 6 ▶

LOS displacement maps for the four interferometric pairs of Table 3. **a** corresponds to the unwrapped and converted to ascending LOS displacement for the 24/08/2016 earthquake, **b** to the ascending LOS displacement for the 26/10/2016 earthquake, **c** to the ascending LOS displacement for the 30/10/2016 earthquake, and **d** to the descending LOS displacement for both the 26/10/2016 and the 30/10/2016 events. A similar displacement pattern is observed for all three ascending displacement maps. West of BB′ is the hanging wall and east of BB′ is the footwall for the 30/10/2016 earthquake

4.2. Triggering of the October 26, 2016 earthquake

We computed Coulomb stress change caused by the August 24, 2016 (Amatrice) event on optimally oriented planes to regional extension. We use the method of "stress on optimal planes" (code STROOP, Simpson and Reasenberg 1994), because all three modeled faults have similar kinematics, i.e., normal slip with predominantly high rake angles, similar geometry with dip angle of 43°–46°, and similar strike of 157°–169° clockwise from north. In addition, all are close in space, i.e., in distances of no more than ~35 km. We expect no significant differences between the codes STROOP and STROP (stress on specific planes) in such tectonic settings. Usually, STROP is used to resolve Coulomb stress on neighboring faults with different kinematics, e.g., on thrust faults in the vicinity of strike–slip faults, where compression is horizontal. For extension azimuth, we adopted the orientation of the extensional axis N70°E determined from the GPS data of D'Agostino et al.

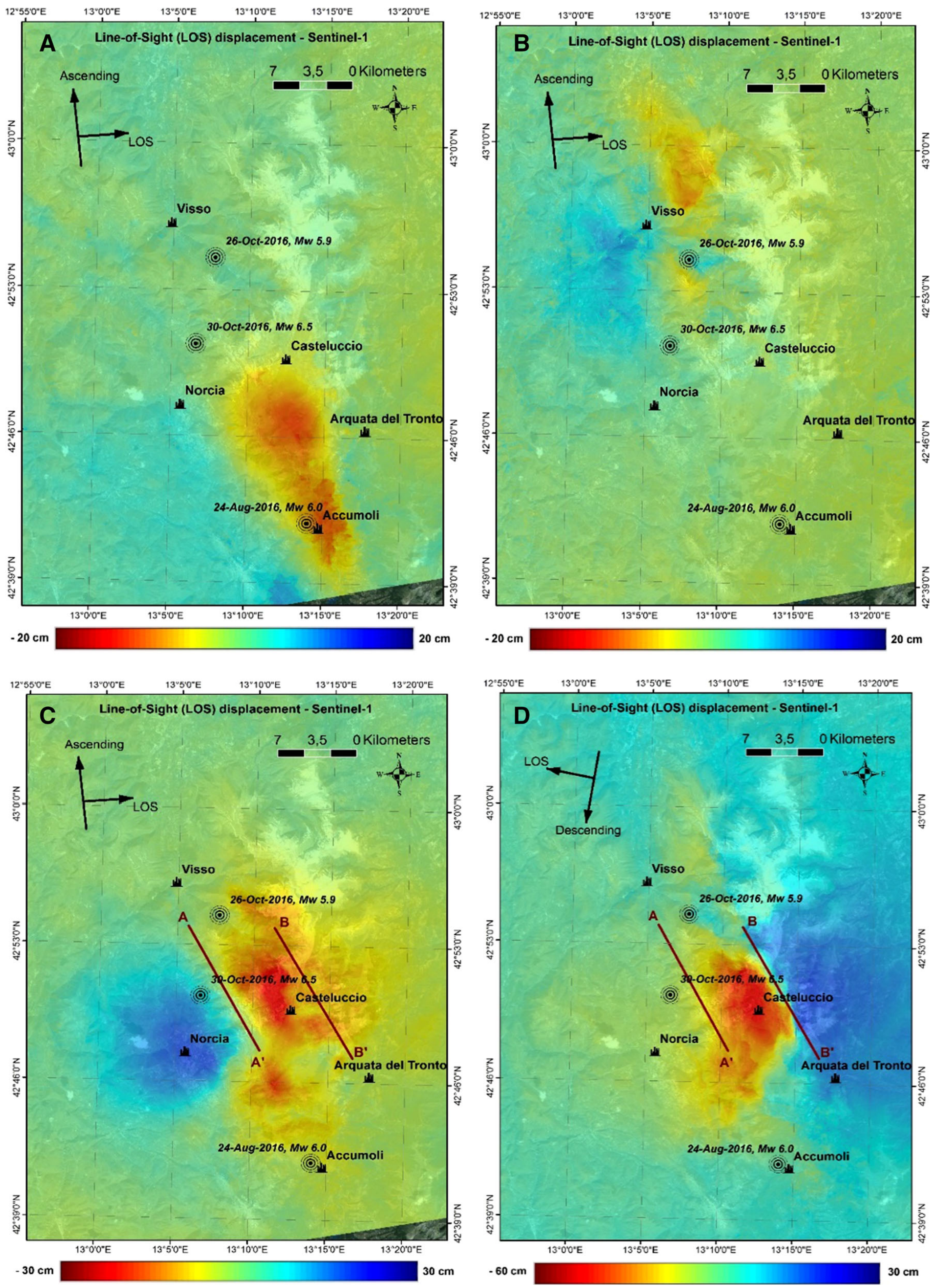
A
Line-of-Sight (LOS) displacement - Sentinel-1
Ascending
LOS
7 3,5 0 Kilometers
Visso
26-Oct-2016, Mw 5.9
30-Oct-2016, Mw 6.5
Casteluccio
Norcia
Arquata del Tronto
24-Aug-2016, Mw 6.0
Accumoli
- 20 cm
20 cm
B
Line-of-Sight (LOS) displacement - Sentinel-1
Ascending
LOS
- 20 cm
20 cm
C
Line-of-Sight (LOS) displacement - Sentinel-1
A
A'
B
B'
- 30 cm
30 cm
D
Line-of-Sight (LOS) displacement - Sentinel-1
LOS
Descending
- 60 cm
30 cm

(2001). This orientation is within 8° from the orientation of the T-axis of the focal plane solution of the October 26, 2016 event (N62°E; Table 4). The calculation was done at depth of 8 km. The target planes are similar in orientation to the October 2016 fault plane, i.e., they strike NNW–SSE and dip either to the W or to the E. The output consists of six grids, one for each component of the tensor. Then, the change in the CFF on optimal failure planes at 8-km depth was calculated by running STROOP. ΔCFF was sampled on a 200 × 200-km grid, with 1-km grid spacing. We estimated an average strike–slip displacement, u_s, of 0.198 m and a dip–slip displacement, u_d, of 0.795 m (the +convention is for

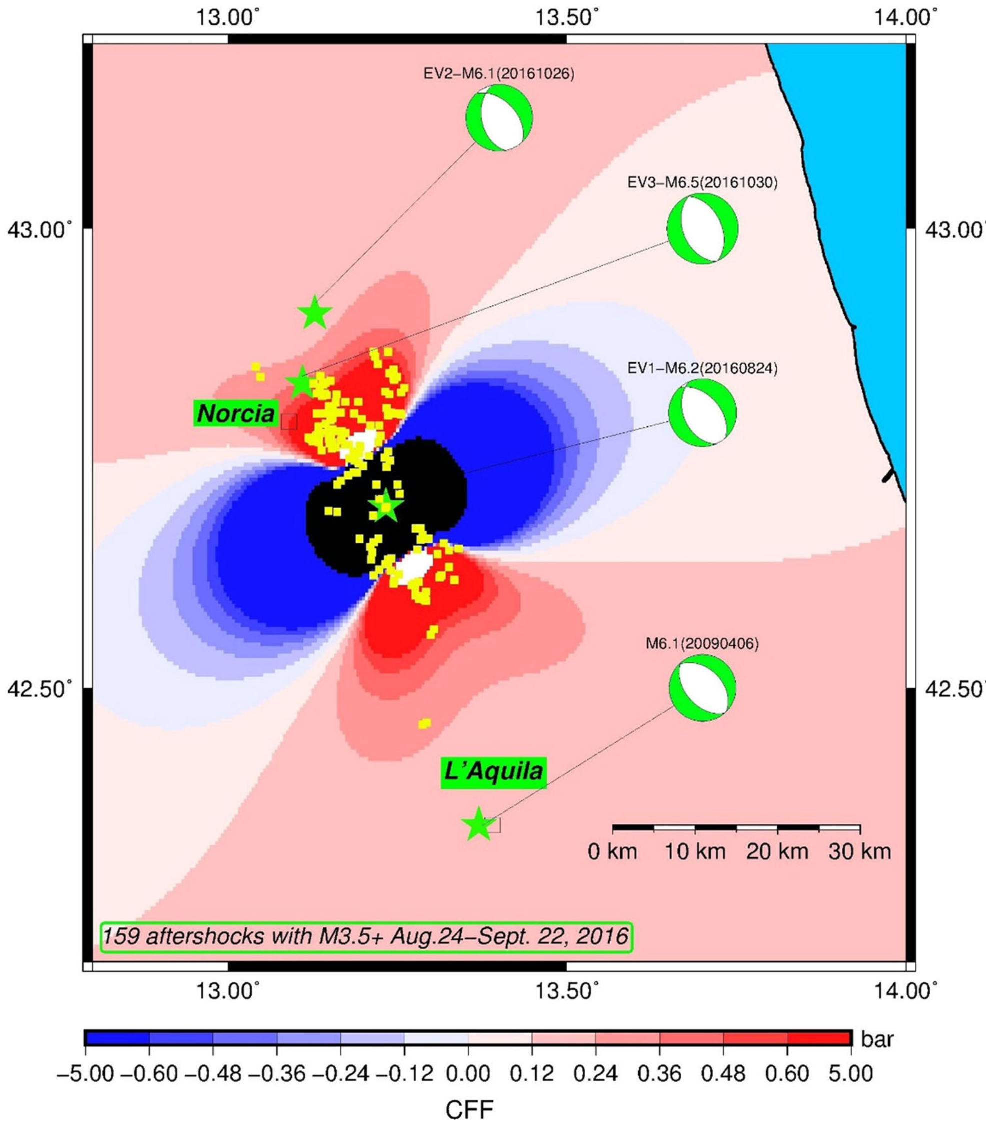

Figure 7
Map of Coulomb stress due to the August 24, 2016 earthquake for optimally oriented faults to regional extension (N70°E) at the depth of 8 km in the case of effective friction 0.4. Colour palette of stress values is linear in the range −0.6 to +0.6 bar (1 bar = 100 kPa). *White colour* indicates area where transferred stress >5 bar. *Yellow stars* show the earthquake epicentres. *Beachballs* indicate moment tensor inversion solutions for mainshocks (*green stars*). *Yellow squares* illustrate aftershock locations by Marchetti et al. (2016)

downward and dextral displacement) for a magnitude M_w 6.2, using the Hanks and Kanamori formula (1979):

$$M_w = (2/3) \times (\log M_o - 16.05), \quad (3)$$

where M_o is the scalar seismic moment of the best double couple in dyne-cm. Seismic moment is given by the following equation:

$$M_o = G \times A \times u, \quad (4)$$

where A is fault area, G is shear modulus, and u is average displacement. We assumed a fault length of 13 km, as determined by our slip inversion, which is also close to the empirical estimate of Wells and Coppersmith (1994) for M_w 6.2 ruptures along normal faults. The fault width was taken 7 km which matches the down-dip size of the larger slip patch of

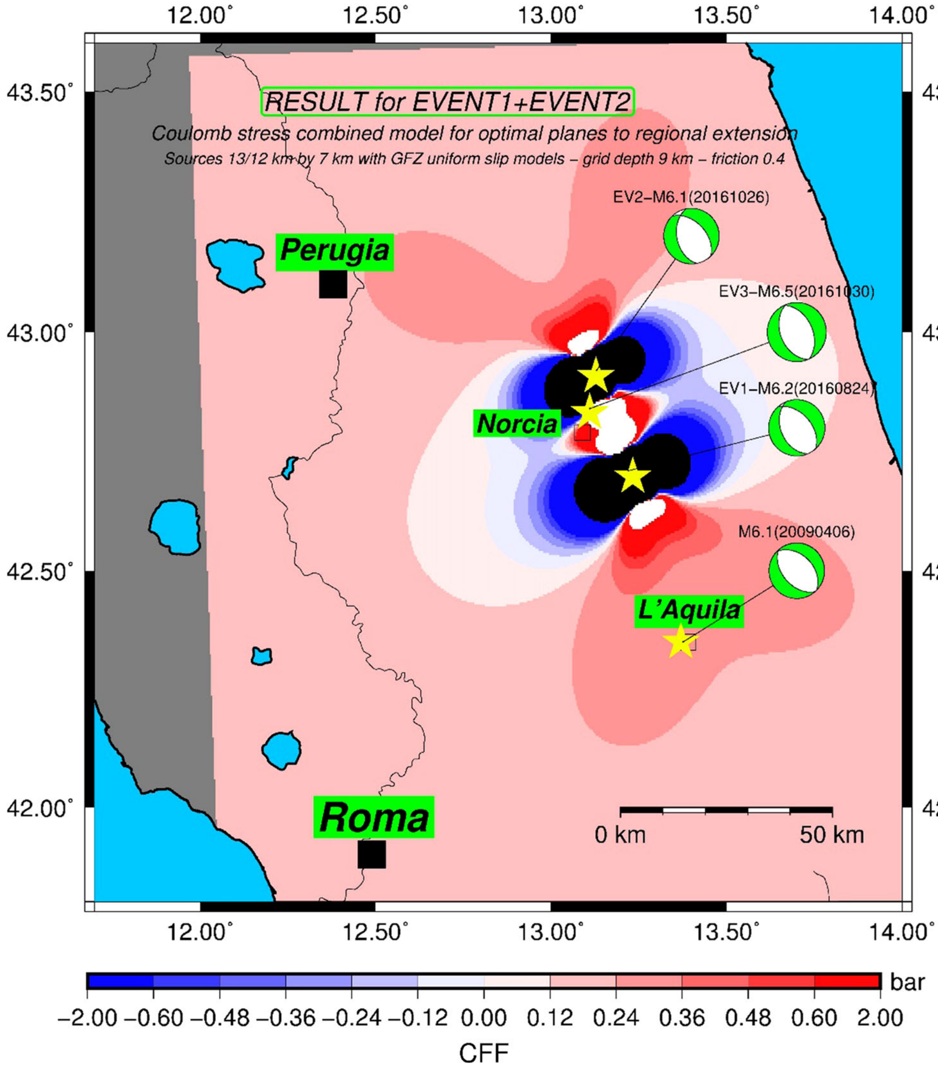

Figure 8

Map of combined ΔCFF for the August 24 and October 26, 2016 earthquakes for optimally oriented faults to regional extension (N70°E) at a depth of 9 km (hypocentral depth of October 30, 2016 event) for friction $\mu' = 0.4$. Colour palette of stress values is linear in the range −0.6 to + 0.6 bar (1 bar = 100 kPa). *Blue areas* indicate unloading, and *red areas* indicate loading. *White colour* indicates area, where transferred stress >2 bar and *black colour* indicates the area, where stress reduction was <−2 bar. *Yellow stars* show the earthquake epicentres both our slip inversion and that of Tinti et al. (2016). The two components of displacement vector were calculated from the following formulas given the slip models, as shown in Table 4:

$$u_s = \cos(\text{rake}) \times u, \tag{5}$$

$$u_d = -\sin(\text{rake}) \times u. \tag{6}$$

The displacement values are assumed to hold for the whole fault surface, i.e., we introduced a uniform slip model. The fault epicentre is set to the dislocation centre, i.e., in the centroid. We also assumed a regional extension loading about 4–10 times the static stress drop of earthquakes in central Italy which ranges between 20 and 50 bars (Rovelli and Calderoni 2014). We modeled the sources as rectangular dislocations, where the slip centroid, i.e., the maximum slip location, is placed at the centre of the rectangle. This is in agreement with the results from the teleseismic inversion on fault-slip patch patterns. The crustal loading parameter of 200 bar is set to satisfy the condition that regional stress used in STROOP modelling is larger than stress drops in Italian earthquakes (20–50 bars). When we model rupture for an M6 earthquake, we generate locally very large stresses, especially at the fault tips, so we need to make sure that our regional, i.e., ambient, stress level is well above the co-seismic stress drops. More explanations can be found in the paper by Ganas et al. (2010).

The uniform slip approach was selected, because it provided a good fit of the fault-slip models to both the kinematic results of the teleseismic inversion and the focal mechanism of the main shock. First, in Coulomb stress modeling, we used the same geometry and kinematics for all three sources with those used in kinematic inversion of teleseismic data (compare Tables 2, 4). Then, we used the depth of 8 km for centroid depth of our slip models (9 km for the Norcia event) as this depth matched satisfactorily the slip maxima of the teleseismic inversion (between 6 and 9 km; see slip distribution in Figs. 3, 4, and 5). Third, all three ruptures were bilateral in their propagation, so the modeled centroid in our analysis (e.g., Figs. 7, 8) is located approximately at the middle of the rectangular source. For example, the event of August 24, 2016 (Amatrice) which ruptured with slip pattern shown in Fig. 3 can be approximated by a rectangular dislocation of dimensions 13 by 7 km (length, width; Table 5), which provides a seismic moment of 2.24×10^{18} Nm or about 2% higher than the value reported in Table 2. Similar arguments are valid for the October 26 and October 30, 2016 events.

The parameters considered for the stress change computation are given in Table 5, while the stress change map is presented in Fig. 7. The October 26, 2016 epicentre (Visso event) is located nearly 25 km to the north of the August 24, 2016 centroid, i.e., about two fault lengths. The Coulomb stress increase along the Visso fault plane (event 2; October 26, 2016) was found +0.19 bar, a value that is considered as capable to trigger an earthquake along an optimally oriented fault (see review by Harris 1998; a small stress perturbation of 0.1 bar can promote failure in some faults). As the resistance to sliding along faults is not the same, it is reasonable to explain the occurrence of the Visso event 4 days before the Norcia (October 30, 2016) event, despite the proximity of the latter to the Amatrice (August 24) event. Assuming similar material properties along both faults, the difference in the activation between the two faults may be related to the time of the penultimate event on each fault, which in turn is related to the stress loading history of each fault. This time may vary from hundreds up to a few 1000 years.

Table 5

Input parameters used for stress-transfer modelling of the August 24, 2016 earthquake

Poisson ratio	0.25
Shear modulus	$G = 300{,}000$ bar
Map projection	UTM zone 33
Depth of ΔCFF calculation	8 km (target is 26/10 hypocenter fault) plane)
Grid size	1 km
Friction coefficient (μ')	0.4
Horizontal length of rupture	13 km
Down-dip length of rupture	7 km
Strike–slip displacement	0.198 m
Dip–slip displacement	0.795 m
Azimuth of extension	N70°E
Regional stress	200 bar (extension)

Furthermore, we calculated a combined Coulomb stress increase of about +2 bar on the fault plane of the Norcia event, which represents a factor of 10 increase with respect to the October 26 event. This was sufficient to overcome the resistance of the fault to failure.

We also investigated the correlation of August 24, 2016 aftershock locations with positive Coulomb stress changes illustrated by red lobes in Fig. 7. We used the aftershock data set published by Marchetti et al. (2016) which comprises 159 well-located crustal events following the M_w 6.2 mainshock for the reporting period from August 24, 2016 to September 22, 2016. All events have local magnitudes of $M_L \geq 3.5$ and most hypocentres are in the 6–10-km range, which is within 2 km of the depth of calculated Coulomb stress changes in our map (Fig. 7). We find strong correlation between aftershock locations and positive stress lobes. Almost all triggered aftershocks are located inside the modeled +0.24 bar contour line. Only 32 aftershocks, a portion of 20% of the data set are located at stress shadows. This result confirms previous studies on effects of Coulomb stress changes on aftershock sequences (e.g., Toda et al. 1998, 2011; Parsons et al. 2012; Ganas et al. 2012, 2013, 2014). Aftershocks that occurred inside the stress shadows could be due to heterogeneous slip that modifies the Coulomb stress-transfer change across the fault, on stress diffusion in the vicinity of the rupture, which may represent a brittle microcracking effect (Scholz 1968), as well as on dynamic stress triggering by body waves (e.g., Kilb et al. 2000).

4.3. Triggering of the October 30, 2016 Earthquake: Combination of the August 24 and October 26 Earthquakes

The next step was to evaluate if the combined stress change due to the events of August 24 and October 26, 2016 can trigger the subsequent event of October 30, 2016. We computed Coulomb stress change, on optimally oriented planes, at hypocentre depth (9 km) of the October 30, 2016 event. The use of optimal planes refers to the regional extension which can have a small deviation from the normal to the strike of the October 30, 2016 fault. The target planes are oriented NNW–SSE, such as the October 30, 2016 fault plane (Table 4). Similarly, ΔCFF was sampled on a horizontal section at 9 km, on a 200 × 200-km grid, with 1 km grid spacing. For the October 26 earthquake of M_w 6.1, we calculated from formulas (4) and (5) average strike–slip and dip–slip displacements of 0.574 and 0.255 m, respectively, while for the August 24 earthquake of M_w 6.2, we inserted the values already calculated earlier: average displacement of 0.198 m for strike–slip and of 0.795 m for dip–slip components. For the October 26, 2016 rupture, we assumed a length of 12 km and a width of 7 km (rupture area 84 km^2), respectively.

Our results (Fig. 8) indicated that the October 30, 2016 event was marginally located inside the area loaded by the combined static stress field, i.e., very close to the boundary between the loaded (calculated load is about +2 bars) and relaxed Coulomb stress lobes. This result implies that the solution is sensitive to the slip model used for the October 26, 2016 event.

4.4. Post-October 30, 2016 Stress Interaction

We also modeled the combined stress field in central Italy due to the occurrence of the October 30, 2016 (Norcia) event (Fig. 9). We computed Coulomb stress change, on optimally oriented planes, at a depth of 8 km. The target planes are oriented NNW–SSE. ΔCFF was sampled on a 200 × 200-km grid, with 1-km grid spacing. Using source dimensions 15 km (length) by 10 km (width), we estimated an average strike–slip displacement of 0.048 m and a dip–slip displacement of 1.401 m for the October 30, 2016 earthquake of magnitude M_w 6.5. Displacements were calculated using Eq. (3). The ΔCFF shape displays a "butterfly" pattern of positive stress lobes with stress loading of more than +0.2 bar along the Apennines, at least 30–50 km on either side of the activated faults. A 100-km-wide relaxation region (shadow zone) has formed across the mountain chain.

The SE lobe of positive stress loading is less extensive than the north–west lobe, covering the area between the epicentres of the strong earthquakes of April 6, 2009 in L'Aquila (M_w 6.3) and of August 26, 2016 (M_w 6.2) in Amatrice (Fig. 9). When writing this paper, a series of strong earthquakes of

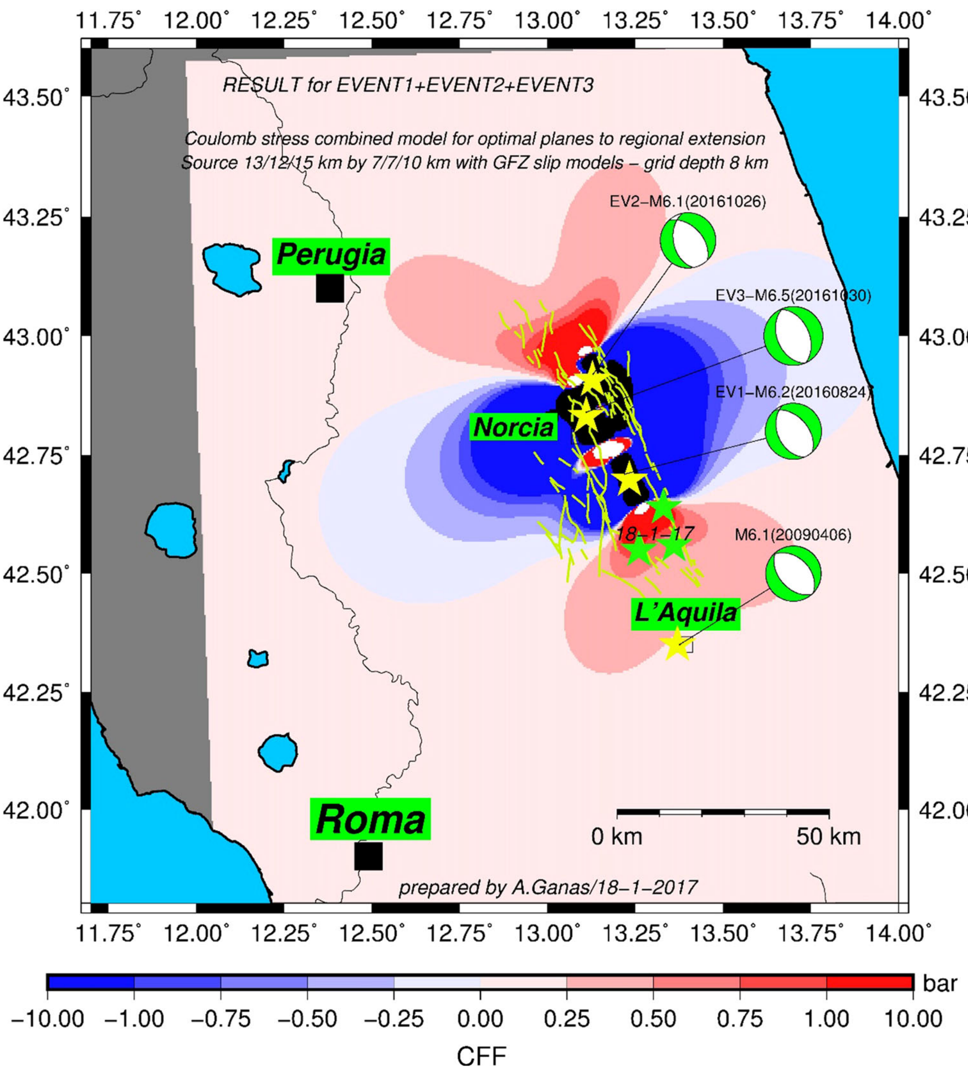

Figure 9
Map of combined ΔCFF for the August 24, October 26, 2016 and October 30, 2016 earthquakes for optimally oriented faults to regional extension (N70°E) at a depth of 8 km for friction $\mu' = 0.4$. Colour palette of stress values is linear in the range -1 to $+1$ bar (1 bar = 100 kPa). *Blue* and *red areas* indicate unloading and loading, respectively. *Yellow stars* show the three strong earthquake epicentres, and *yellow lines* are active faults after Roberts and Michetti (2004). *Green stars* show the epicentres of the earthquakes that occurred on January 18, 2017 with magnitudes M_w 5.3, 5.7, and 5.6

magnitudes 5.3, 5.7, and 5.6 occurred exactly within the area covered by the SE lobe, thus verifying that the seismic potential was still high after the October 30, 2016 earthquake. The potential remaining for strong earthquake generation is further discussed in Sect. 5 by taking into account the stress increase produced also by the L'Aquila mainshock of 2009. On the other side, the NW lobe of positive stress loading occupies an area, where significant seismic potential was concentrated. With the exception of the September 26, 1997 earthquake of M_w 6.0, no other strong earthquake of magnitude over 6.0 ruptured there since AD 1328. This indicates that the potential for strong earthquake generation may also have increased due to the stress loading after the October 30, 2016 earthquake.

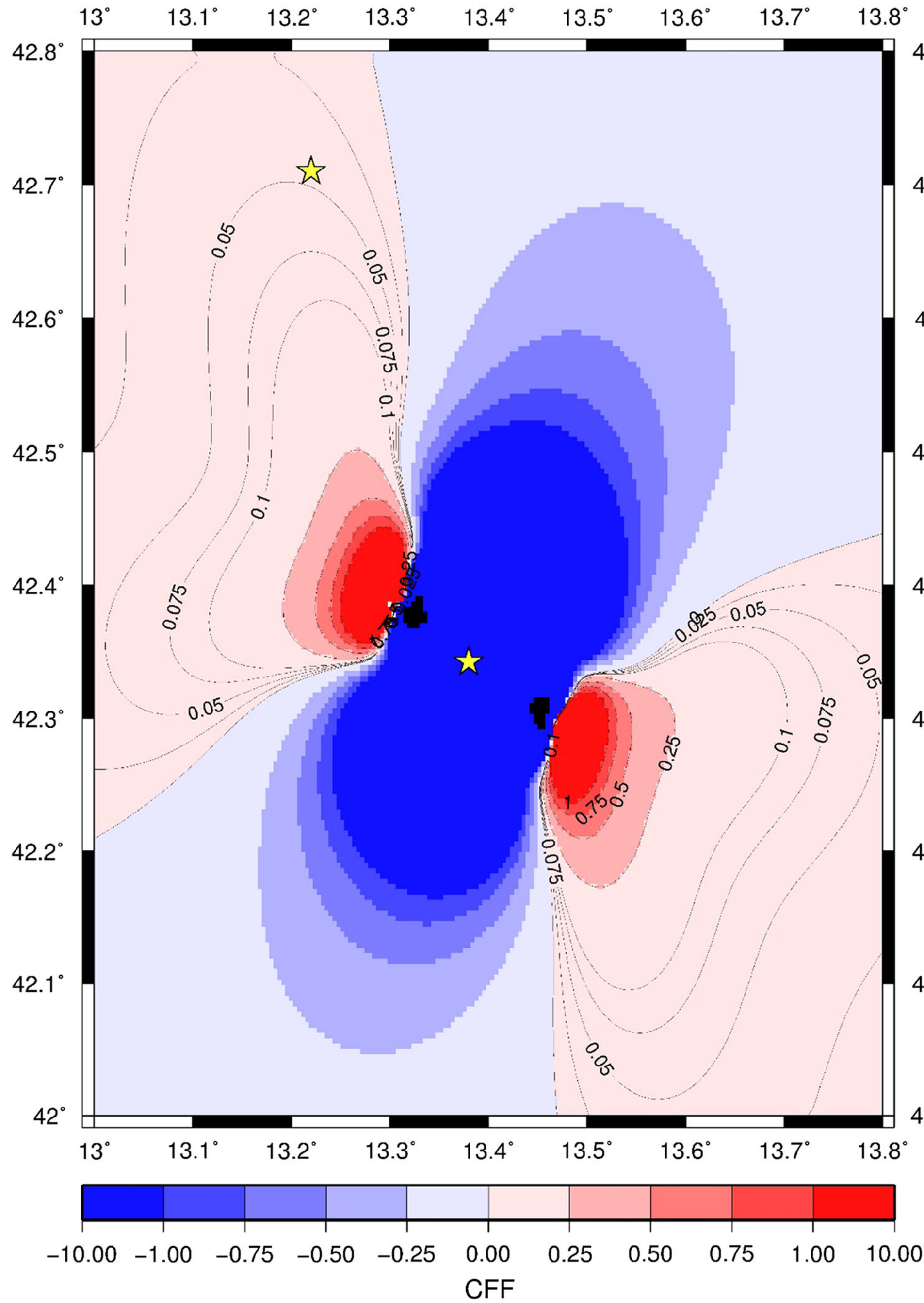

Figure 10
Map of ΔCFF contours for the April 6, 2009 earthquake of L'Aquila (south star); north star is the epicentre of the Amatrice earthquake of August 24, 2016

5. *Discussion and Conclusions*

The inversion of P waves recorded at teleseismic distances showed that the three, normal faulting very strong earthquakes occurring sequentially in Central Apennines on August 24 (event 1, Amartice), October 26 (event 2, Visso), and October 30 (event 3, Norcia), 2016, had seismic moments of 2.2×10^{18},

1.8×10^{18}, and 6.6×10^{18} Nm corresponding to moment magnitudes of 6.2, 6.1, and 6.5, respectively. These values are absolutely consistent with magnitudes determined by various seismological centers (Table 1). Event 1 had seismic slip $s = 1.2$ m in the hypocenter and $s' = 0.3$ m near the surface, while values of $s = 0.8$ m, $s' = 0.1$ m and $s = 1.4$ m, $s' = 0.7$ m were found for events 2 and 3, respectively. The respective fault lengths were calculated at about 13, 12, and 17 km. The values calculated for the seismic slip near the surface are close to the ones received from DInSAR analysis for the maximum ground subsidence: 0.2, 0.15, and 0.35 m, for events 1, 2, and 3, respectively. The combined results received by the inversion of teleseismic P-wave records, measurements of DInSAR Sentinel 1 and 2 satellite images, and Coulomb stress-transfer modelling provided strong evidence for earthquake triggering effects in the sequence of the three very strong earthquakes in Central Apennines.

Quite similar DInSAR displacement patterns became evident for the three earthquakes which indicate that these earthquakes likely had common faulting mode and geometry as it became evident from fault-plane solutions (Table 2). P-wave inversion revealed that bilateral rupture was also a common feature of the three events. However, predominant directivity was observed towards NW and SSE due to events 1 and 2, respectively. This result implies that the area of event 2 was possibly stressed due to event 1 and that event 3, which was the largest in the sequence, and very likely was stressed due to the occurrence of the two previous earthquakes. DInSAR measurements showed also ground deformation directivity from events 1 and 2 towards event 3.

Strong evidence for earthquake triggering effects was provided by Coulomb stress-transfer modelling. The second earthquake of October 26, 2016 in Visso area was likely triggered by the August 24, 2016 event (Amatrice), because it occurred along a normal fault plane with optimal orientation to regional extension and was loaded by a positive amount of ~ 0.19 bars. Furthermore, the largest event of October 30, 2016 in Norcia area was stressed by a positive amount of about 2 bars due to the combined stress transfer by events 1 and 2. Therefore, we suggest that very likely, this event was triggered from the cumulative effect of the two previous events, despite its proximity to the negative/positive lobe boundary. The sequence of events in a time difference of ~ 2 months, epicentre distance of ~ 25 km between events 1 and 2, and 8.5 km between events 2 and 3, in association with the static stress-transfer model demonstrates the so-called "domino-effect" in the earthquake occurrence.

The cumulative Coulomb stress change caused by the three very strong large earthquakes showed a "butterfly" pattern of positive stress lobes with stress loading of more than 0.50 bars along the Apennines to the NW and SE of the entire activated zone. On the other hand, a relaxation or shadow zone has formed across the mountain chain. The SE lobe of positive stress loading occupies the area to the south of the August 26, 2016 (M_w 6.2) Amatrice earthquake up to the epicentre of the April 6, 2009 L'Aquila earthquake (M_w 6.3). On January 18, 2018, a series of strong earthquakes measuring magnitudes 5.3, 5.7, and 5.6 occurred within the area of the SE positive stress lobe. This is an evidence that the seismic potential increased in the area after the three very strong events of 2016 and that this favored earthquake triggering effect. Due to the relaxation produced by the series of strong earthquakes of January 18, 2017, and because the stressed area is not very extensive, one may argue at first approximation that the seismic potential for the occurrence of more strong earthquakes has reduced. However, by considering that the cumulative magnitude of this series of earthquakes is only ~ 5.88, as calculated from formula (2), we may consider that significant seismic potential remains in the area covered by the SE lobe of stress increase. This is further supported by the DCFF field produced by the L'Aquila mainshock (M_w 6.3) of April 6, 2016 (Fig. 10). Although it seems that the 2009 did not triggered the Amatrice earthquake of August 24, 2016, the stress increased in the area, where additional increase was accumulated by the last earthquake. We do not suggest that the 2016 sequence was triggered by the 2009 L'Aquila event. However, our combined 2016 stress-transfer models (Fig. 9) predict Coulomb stress increase (at least 0.25 bar) in the region south of the Amatrice, which was already loaded by the 2009 event (because of the favourable orientation of the latter). Therefore, in the region between Amatrice and L'Aquila, the 2016 events imparted stress loading in addition to the 2009 event. On the other hand, the NW lobe of positive stress loading occupies a more extensive area. In addition, since AD 1328, only a M_w 6.0 earthquake ruptured there on September 26, 1997. This indicates that the potential for strong earthquake occurrence increased after the three 2016 very strong earthquakes and that important seismic potential has been accumulated.

Acknowledgements

This work was supported by the Center of Excellence BEYOND ("Building a Centre of Excellence for EO-based monitoring of Natural Disasters"), funded by the EU-FP7-REGPOT-2012-2013-1, G.A. 316210 project. This is also a contribution to the internal research project EARTHWARN of the Institute of Geodynamics, National Observatory of Athens (NOA). We acknowledge Bob Simpson for making available the DLC code. Ch. Kyriakopoulos, S. Valkaniotis, and Ch. Tsimi helped with Italian geophysical data. Thanks are due to Gian Maria Bocchini, PhD student at NOA, for useful discussions on the tectonics of Apennines. All illustrations were prepared using the GMT software (Wessel et al. 2013). We thank two anonymous reviewers for their constructive comments which helped to improve substantially the initial manuscript.

Appendix

See Figs. 11, 12, and 13.

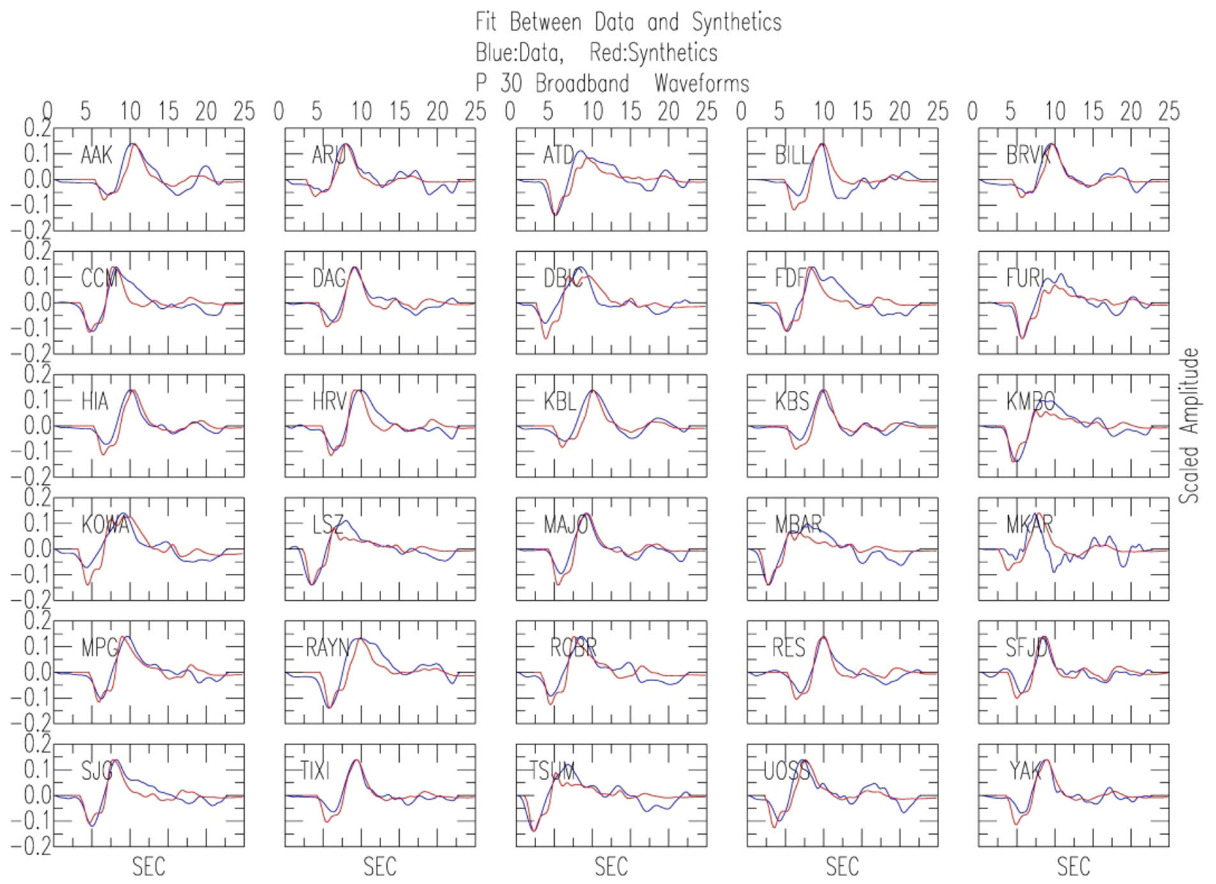

Figure 11
Fit between the records and the synthetics for the earthquake of August 24, 2016

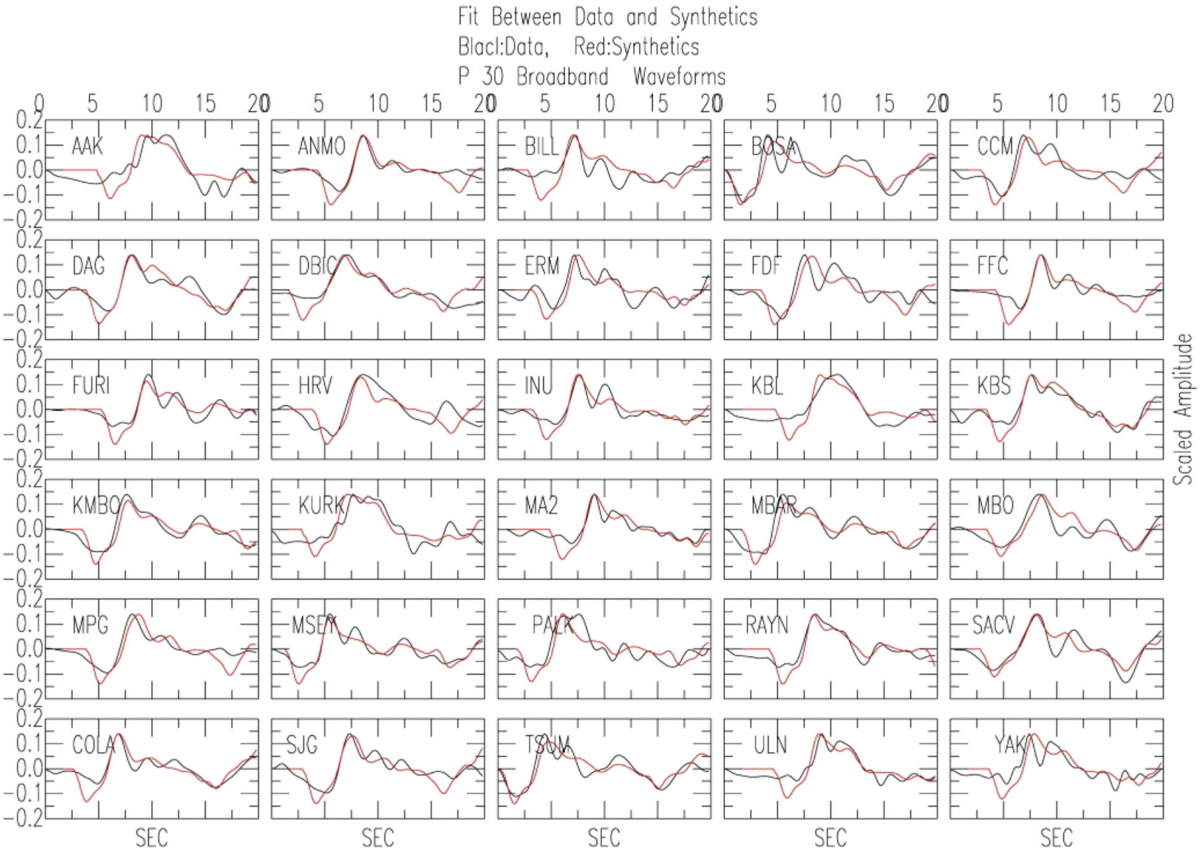

Figure 12
As shown in Fig. 11 for the earthquake of October 26, 2016

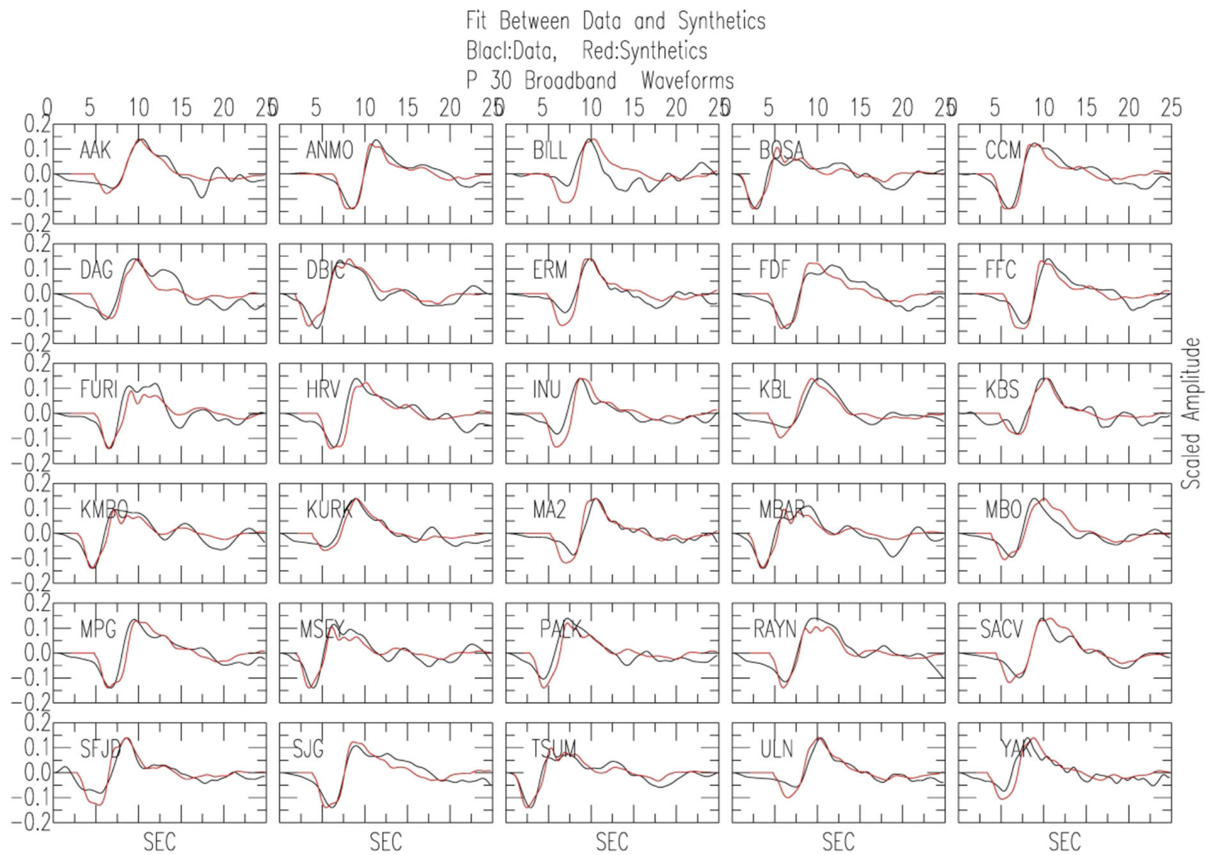

Figure 13
As shown in Fig. 11 for the earthquake of October 30, 2016

References

Albano, M., Saroli, M., Moro, M., Falcucci, E., Gori, S., Stramondo, S., et al. (2016). Minor shallow gravitational component on the Mt. Vettore surface ruptures related to M_w 6, 2016 Amatrice earthquake. *Annals of Geophysics, 59, Fast Track 5,* 1–6. doi:10.4401/ag-7299.

Avallone, A., Latorre, D., Serpelloni, E., Cavaliere, A., Herrero, A., Cecere, G., et al. (2016). Coseismic displacement waveforms for the 2016 August 24 M_w 6.0 Amatrice earthquake (central Italy) carried out from high-rate GPS data. *Annals of Geophysics, 59,* Fast Track 5. doi:10.4401/ag-7275.

Basili, R., & Meghraoui, M. (2001). Coseismic and postseismic displacements related with 1997 earthquake sequence in Umbria–Marche (central Italy). *Geophysical Research Letters, 28*(14), 2695–2698.

Bignami, C., Tolomei, C., Pezzo, G., Guglielmino, F., Atzori, S., Trasatti, E., et al. (2016). Source identification for situational awareness of August 24th 2016 central Italy event. *Annals of Geophysics, 59,* Fast Track 5. doi:10.4401/AG-7233.

Boncori, J. P. M., Papoutsis, I., Pezzo, G., Tolomei, C., Atzori, S., Ganas, A., et al. (2015). The February 2014 Cephalonia earthquake (Greece): 3D deformation field and source modeling from multiple SAR techniques. *Seismological Society of America, 86*(1), 124–137. doi:10.1785/0220140126. **(early edition)**.

Bonini, L., Maesano, F. E., Basili, R., Burrato, P., Cosimo Carafa, M. M., Fracassi, U., et al. (2016). Imaging the tectonic framework of the 24 August 2016, Amatrice (central Italy) earthquake sequence: New roles for old players? *Annals of Geophysics, 59,* Fast Track. doi:10.4401/ag-7229.

Cocco, M., Nostro, C., & Ekström, G. (2000). Static stress changes and fault interaction during the 1997 Umbria–Marche earthquake sequence. *Journal of Seismology, 4,* 501–516.

Costantini, M. (1998). A novel phase unwrapping method based on network programming. *IEEE Transactions on Geoscience and Remote Sensing, 36*(3), 813–821. doi:10.1109/36.673674.

D'Agostino, N., Giuliani, R., Mattone, M., & Bonci, L. (2001). Active crustal extension in the Central Apennines (Italy) inferred from GPS measurements in the interval 1994–1999. *Geophysical Research Letters.* doi:10.1029/2000GL012462.

Dalla Via, G., De Natale, G., Troise, C., Pingue, F., Obrizzo, F., Riva, R., et al. (2003). First evidence of post seismic deformation in the central Mediterranean: Crustal viscoelastic relaxation in the area of the 1980 Irpinia earthquake (Southern Italy). *Geophysical Journal International, 154,* F9–F14.

Falcucci, E., Gori, S., Galadini, F., Fubelli, G., Moro, M., & Saroli, M. (2016). Active faults in the epicentral and mesoseismal M_L

6.0 August 24, 2016 Amatrice earthquake region, central Italy. Methodological and seismotectonic issues. *Annals of Geophysics, 59,* Fast Track 5. doi:10.4401/ag-7266.

Farr, T. G., & Kobrick, M. (2000). Shuttle radar topography mission produces a wealth of data. *EOS Transactions of the American Geophysical Union, 81,* 583–585.

Freed, A. M. (2005). Earthquake triggering by static, dynamic, and postseismic stress transfer. *Annual Review of Earth and Planetary Sciences*. doi:10.1146/annurev.earth.33.092203.122505.

Ganas, A., Chousianitis, K., Batsi, E., Kolligri, M., Agalos, A., Chouliaras, G., et al. (2013). The January 2010 Efpalion earthquakes (Gulf of Corinth, Central Greece): Earthquake interactions and blind normal faulting. *Journal of Seismology, 17*(2), 465–484.

Ganas, A., Gosar, A., & Drakatos, G. (2008). Static stress changes due to the 1998 and 2004 Krn Mountain (Slovenia) earthquakes and implications for future seismicity. *Natural Hazards and Earth System Sciences, 8,* 59–66.

Ganas, A., Grecu, B., Batsi, E., & Radulian, M. (2010). Vrancea slab earthquakes triggered by static stress transfer. *Natural Hazards and Earth Systems Sciences, 10,* 2565–2577.

Ganas, A., Roumelioti, Z., & Chousianitis, K. (2012). Static stress transfer from the May 20, 2012, M6.1 Emilia-Romagna (northern Italy) earthquake using a co-seismic slip distribution model. *Annals of Geophysics, 55*(4), 655–666.

Ganas, A., Roumelioti, Z., Karastathis, V., Chousianitis, K., Moshou, A., & Mouzakiotis, E. (2014). The Lemnos 8 January 2013 ($M_w = 5.7$) earthquake: Fault slip, aftershock properties and static stress transfer modeling in the north Aegean Sea. *Journal of Seismology, 18*(3), 433–455.

Goldstein, R. M., & Werner, C. L. (1998). Radar interferogram filtering for geophysical applications. *Geophysical Research Letters, 25*(21), 4035–4038. doi:10.1029/1998GL900033.

Gomberg, J., Reasenberg, P. A., Bodin, P., & Harris, R. A. (2001). Earthquake triggering by seismic waves following the Landers and Hector mine earthquakes. *Nature, 411,* 462–466.

Hanks, T. C., & Kanamori, H. (1979). A moment magnitude scale. *Journal of Geophysical Research, 84,* 2348–2350.

Harris, R. A. (1998). Introduction to special section: Stress triggers, stress shadows, and implications for seismic hazard. *Journal of Geophysical Research, 103,* 24347–24358.

Harris, R. A., Simpson, R. W., & Reasenberg, P. A. (1995). Influence of static stress changes on earthquake locations in southern California. *Nature, 375,* 221–224.

Hartzell, S. H., & Heaton, T. H. (1983). Inversion of strong ground motion and teleseismic waveform data for the fault rupture history of the 1979 Imperial Valley, California, earthquake. *Bulletin of the Seismological Society of America, 73,* 1553–1583.

Hartzell, S. H., & Langer, Ch. (1993). Importance of model parameterization in finite fault inversions: Application to the 1974 M_w 8.0 Peru earthquake. *Journal of Geophysical Research, 98,* 22123–22134.

Hartzell, S. H., Pengcheng, L., & Mendoza, C. (1996). The 1994 Northridge, California earthquake: Investigation of rupture velocity, rise time and high-frequency radiation. *Journal of Geophysical Research, 101,* 20091–20108.

Heaton, T. H. (1982). The 1971 San Fernando earthquake: A double event? *Bulletin of the Seismological Society of America, 72,* 2037–2062.

Herrmann, R. B., Malagnini, L., & Munafò, I. (2011). Regional moment tensors of the 2009 L'Aquila earthquake sequence. *Bulletin of the Seismological Society of America, 101,* 975–993.

Huang, M. -H., Fielding, E. J., Liang, C., Milillo, P., Bekaert, D., Dreger, D., & Salzer, J. (2017). Coseismic deformation and triggered landslides of the 2016 Mw 6.2 Amatrice earthquake in Italy. *Geophysical Research Letters, 44*, 1266–1274. doi:10.1002/2016GL071687.

Jacques, E., Monaco, C., Tapponnier, P., Tartorici, L., & Winter, T. (2001). Faulting and earthquake triggering during the 1783 Calabria seismic sequence. *Geophysical Journal International, 147,* 499–516.

Kilb, D., Gomberg, J., & Bodin, P. (2000). Triggering of earthquake aftershocks by dynamic stresses. *Nature, 408,* 570–574.

Langston, C. A., & Helmberger, D. V. (1975). A procedure for modeling shallow dislocation sources. *Geophysics Journal of the Royal Astronomical Society, 42,* 117–130.

Lanzano, G., Luzi, L., Pacor, F., Puglia, R., D'Amico, M., Felicetta, C., et al. (2016). Preliminary analysis of the accelerometric recordings of the August 24th, 2016 MW 6.0 Amatrice earthquake. *Annals of Geophysics, 59,* Fast Track 5. doi:10.4401/ag-7201.

Lavecchia, G., et al. (2016). Ground deformation and source geometry of the 24 August 2016 Amatrice earthquake (Central Italy) investigated through analytical and numerical modeling of DInSAR measurements and structural-geological data. *Geophysical Research Letters, 43,* 12389–12398. doi:10.1002/2016GL071723.

Louvari, E., & Kiratzi, A. (1997). Rake: A window's program to plot earthquake focal mechanisms and stress orientation. *Computers and Geosciences, 23,* 851–857.

Marchetti, A., et al. (2016). The Italian Seismic Bulletin: Strategies, revised pickings and locations of the central Italy seismic sequence. *Annals of Geophysics*. doi:10.4401/ag-7169.

Mendoza, C., & Hartzell, S. (2013). Finite-Fault source inversion using teleseismic P waves: Simple parameterization and rapid analysis. *Bulletin of the Seismological Society of America, 103,* 834–844.

Murru, M., Taroni, M., Akinci, A., & Falcone, G. (2016). What is the impact of the August 24, 2016 Amatrice earthquake on the seismic hazard assessment in central Italy? *Annals of Geophysics*. doi:10.4401/AG-7209.

Okada, Y. (1992). Internal deformation due to shear and tensile faults in a half-space. *Bulletin of the Seismological Society of America, 82,* 1018–1040.

Pace, P., & Calamita, F. (2014). Push-up inversion structures vs. fault-bend reactivation anticlines along oblique thrust ramps: Examples from the Apennines fold-and-thrust belt (Italy). *Journal of the Geological Society, 171,* 227–238. doi:10.1144/0016-76492013-053.

Parsons, T., Ogata, Y., Zhuang, J., & Geist, E. L. (2012). Evaluation of static stress change forecasting with prospective and blind tests. *Geophysical Journal International, 188,* 1425–1440. doi:10.1111/j.1365-246X.2011.05343.x.

Parsons, T., Yeats, R. S., Yagi, Y., & Hussain, A. (2006). Static stress change from 8 October, 2005 M = 7.6 Kashmir earthquake. *Geophysical Research Letters, 33,* L06304. doi:10.1029/2005GL025429.

Perniola, B., Bressan, G., & Pondrelli, S. (2003). Changes in failure stress and stress transfer during the 1976–1977 Friuli earthquake sequence. *Geophysical Journal International, 156,* 297–306. doi:10.1111/j.1365-246X.2003.02146.x.

Pischiutta, M., Akinci, A., Malagnini, L., & Herrero, A. (2016). Characteristics of the Strong Ground Motion from the 24th

August 2016 Amatrice Earthquake. *Annals of Geophysics, 59,* Fast Track 5. doi:10.4401/AG-7219.

Pondrelli, S., Salimbeni, S., & Perfetti, P. (2016). Moment tensor solutions for the Amatrice 2016 seismic sequence. *Annals of Geophysics, 59,* Fast Track 5. doi:10.4401/ag-7240.

Pucci, S., et al. (2016). Coseismic effects of the 2016 Amatrice seismic sequence: First geological results. *Annals of Geophysics, 59, Fast Track 5,* 1–8. doi:10.4401/AG-7195.

Reasenberg, P. A., & Simpson, R. W. (1992). Response of regional seismicity to the static stress change produced by Loma Prieta earthquake. *Science, 255,* 1687–1690.

Riva, R., Aoudia, A., Vermeersen, L. L. A., Sabadini, R., & Panza, G. F. (2000). Crustal versus asthenospheric relaxation and post-seismic deformation for shallow normal faulting earthquakes: The Umbria-Marche (central Italy) case. *Geophysical Journal International, 141,* F7–F11.

Roberts, G. P., & Michetti, A. M. (2004). Spatial and temporal variations in growth rates along active normal fault systems: An example from Lazio-Abruzzo, central Italy. *Journal of Structural Geology, 26,* 339–376.

Rovelli, A., & Calderoni, G. (2014). Stress drops of the 1997–1998 Colfiorito, Central Italy Earthquakes: Hints for a common behaviour of normal faults in the Apennines. *Pure and Applied Geophysics, 171,* 2731. doi:10.1007/s00024-014-0856-1.

Rovida, A., Locati, M., Camassi, R., Lolli, B., & Gasperini, P. (2016). CPTI15, the 2015 version of the Parametric Catalogue of Italian Earthquakes. *Istituto Nazionale di Geofisica e Vulcanologia*. doi:10.6092/INGV.IT-CPTI15.

Saccorotti, G., Piccinini, D., & Giunchi, C. (2016). Rupture imaging for the 2016 August 24, M_w = 6.0 central Italy earthquake, from back projection of strong motion array data. *Annals of Geophysics, 59,* Fast Track 5. doi:10.4401/AG7294.

Scholz, C. H. (1968). Microfractures, aftershocks and seismicity. *Bulletin of the Seismological Society of America, 58,* 1117–1130.

Simpson R. W., & Reasenberg, P. A. (1994). Earthquake-induced static-stress changes on central California Faults. In: R. W. Simpson (Ed.), *U.S. geological survey professional paper 1550-F "The Loma Prieta, California, Earthquake of October 17, 1989—Tectonic Processes and Models*", p 134.

Somerville, P., Irikura, K., Graves, R., Sawada, S., Wald, D., Abrahamson, N., et al. (1999). Characterizing crustal earthquake slip models for the prediction of strong ground motion. *Seismological Research Letters, 70,* 59–80.

Stein, R. S., Barka, A. A., & Dietrich, J. H. (1997). Progressive failure on the North Anatolian fault since by 1939 by earthquake stress triggering. *Geophysical Journal International, 128,* 594–604.

Stein, S., & Wysession, M. (2003). *An introduction to seismology, earthquakes, and earth structure* (p. 498). Oxford: Blackwell Publishers.

Tinti, E., Scognamiglio, L., Michelini, A., & Cocco, M. (2016). Slip heterogeneity and directivity of the M_L 6.0, 2016, Amatrice earthquake estimated with rapid finite-fault inversion. *Geophysical Research Letters*. doi:10.1002/2016GL071263.

Toda, S., Stein, R. S., & Lin, J. (2011). Widespread seismicity excitation throughout central Japan following the 2011 M = 9.0 Tohoku earthquake and its interpretation by Coulomb stress transfer. *Geophysical Research Letters, 38,* L00G03. doi:10.1029/2011GL047834.

Toda, S., Stein, R. S., Reasenberg, P. A., & Dieterich, J. H. (1998). Stress transferred by the M_w = 6.5 Kobe, Japan, shock: Effect on aftershocks and future earthquake probabilities. *Journal of Geophysical Research, 103,* 24543–24565.

Wells, D. L., & Coppersmith, K. J. (1994). New empirical relationships among magnitude, rupture length, rupture width, rupture area and surface displacement. *Bulletin of the Seismological Society of America, 84*(4), 974–1002.

Wessel, P., Smith, W. H. F., Scharroo, R., Luis, J. F., & Wobbe, F. (2013). Generic mapping tools: Improved version released. *EOS Transactions of the American Geophysical Union, 94,* 409–410.

(Received February 1, 2017, revised June 17, 2017, accepted June 28, 2017)